ADVANCED FUNCTIONAL MATERIALS
www.afm-journal.de

The Role of Chemical Composition in Determining the Charge-Carrier Dynamics in (AgI)x(BiI3)y Rudorffites

*Snigdha Lal, Marcello Righetto, Benjamin W. J. Putland, Harry C. Sansom, Silvia G. Motti, Heon Jin, Michael B. Johnston, Henry J. Snaith, and Laura M. Herz**

Silver-bismuth-based perovskite-inspired materials (PIMs) are increasingly being explored as non-toxic materials in photovoltaic applications. However, many of these materials exhibit an ultrafast localization of photogenerated charge carriers that is detrimental for charge-carrier extraction. In this work, such localization processes are explored for thermally evaporated thin films of compositions lying along the $(AgI)_x(BiI_3)_y$ series, namely BiI_3, $AgBi_2I_7$, $AgBiI_4$, Ag_2BiI_5, Ag_3BiI_6, and AgI, to investigate the impact of changing Ag^+/Bi^{3+} content. A persistent presence of ultrafast charge-carrier localization in all mixed compositions and BiI_3, together with unusually broad photoluminescence spectra, reveal that eliminating silver will not suppress the emergence of a localized state. A weak change in electronic bandgap and charge-carrier mobility reveals the resilience of the electronic band structure upon modifications in the Ag^+/Bi^{3+} composition of the mixed-metal rudorffites. Instead, chemical composition impacts the charge-carrier dynamics indirectly via structural alterations: Ag-deficient compositions demonstrate stronger charge-carrier localization most likely because a higher density of vacant sites in the cationic sublattice imparts enhanced lattice softness. Unraveling such delicate interplay between chemical composition, crystal structure, and charge-carrier dynamics in $(AgI)_x(BiI_3)_y$ rudorffites provides crucial insights for developing a material-by-design approach in the quest for highly efficient Bi-based PIMs.

1. Introduction

The unprecedented success of lead halide perovskite (LHP) based solar cells, now yielding power conversion efficiencies (PCE) exceeding 26%,[1–4] has created a new paradigm for emergent photovoltaic (PV) applications. However, concerns around poor stability and toxicity of LHPs, as well as the urgency of developing efficient and stable wider-bandgap semiconductors for tandem solar cell applications,[5–9] have catalyzed the study of alternative metal halide semiconductors. In recent years, chemical intuition has guided the exploration across the vast compositional space of emerging semiconductors: on the one hand, the poor thermal stability associated with the presence of volatile organic cations [10,11] has raised the interest in all-inorganic materials.[12–15] On the other hand, due to the perceived toxicity of lead, the search for lead-free photo absorber materials continues to attract significant attention in this domain.[12,16–19]

Within this compositional space, bismuth-based semiconductors have emerged as a promising alternative to LHPs. Bi^{3+} is non-toxic and shares with Pb^{2+} the so-called "lone pair" ns^2np^0 valence shell configuration, associated with strong band-edge absorption, low charge-carrier effective masses, and defect tolerance exhibited by LHPs.[20–23] Given the aliovalent nature of bismuth as compared to lead (Bi^{3+} compared to Pb^{2+}), it cannot directly substitute lead in a perovskite crystal structure owing to net electronic neutrality requirements. Instead, Bi-based semiconductors crystallize in a variety of modified crystal structures, collectively referred to as perovskite-inspired materials (PIMs).[17] In PIMs, the common octahedral halogenometallate $[MX_6]$ motif condenses into 3D or low-dimensional networks through corner, edge- or face-sharing connections, where charge-balance constraints are generally satisfied through alloying with aliovalent metal substituents (like Ag^+ or Cu^+) or through structurally incorporated deficiencies (i.e., vacant cationic sublattice sites). The resultant PIMs can be broadly classified into two categories: i) crystal structures with reduced structural dimensionality (as in the case of $A_3Bi_2I_9$ where A can be K^+, Rb^+, Cs^+, MA^+ or FA^+),[21,24] or ii) multinary compositions consisting of alternating $[MX_6]^{5-}$ and $[BiX_6]^{3-}$ octahedra as in the case of double perovskites and rudorffites.[21,25,26] The large

S. Lal, M. Righetto, B. W. J. Putland, H. C. Sansom, S. G. Motti, H. Jin, M. B. Johnston, H. J. Snaith, L. M. Herz
Department of Physics
Clarendon Laboratory
University of Oxford
Parks Road, Oxford OX1 3PU, UK
E-mail: laura.herz@physics.ox.ac.uk

S. G. Motti
School of Physics and Astronomy
Faculty of Engineering and Physical Sciences
University of Southampton
University Road, Southampton SO17 1BJ, UK

L. M. Herz
Institute for Advanced Study
Technical University of Munich
Lichtenbergstrasse 2a, 85748 Garching, Germany

The ORCID identification number(s) for the author(s) of this article can be found under https://doi.org/10.1002/adfm.202315942

DOI: 10.1002/adfm.202315942

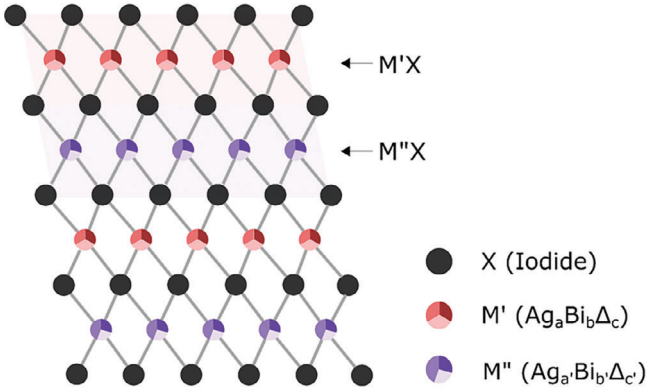

Figure 1. Schematic illustration of the structure of mixed Ag-Bi iodides. The diagram shows a 2D rendition of the edge-sharing octahedral network with the black spheres representing the anionic sublattice, and colored spheres the cationic sublattice. The dual color scheme of the cationic sublattice is used to differentiate between the layers M'X and M"X. Each colored sphere is further divided into three segments which represents the population distributions of Ag, Bi and vacant sites Δ. The population distribution at the cation lattice site varies between the two layers and is shown by changing the ratio of segmentation of the colored spheres.

effective charge-carrier masses and low defect formation energies for deep traps in dimensionally reduced $A_3Bi_2I_9$ have been shown to underlie the unremarkable PCEs reported for solar cells based on this light absorber material.[21,27] On the other hand, while enhanced thermal stability [28,29] and long charge-carrier diffusion lengths have been reported for Ag-Bi double perovskites such as $Cs_2AgBiBr_6$,[30,31] their indirect bandgap and the higher-lying direct transition in the UV make this material less suitable for PV applications.[32] Despite exhibiting optically-allowed direct transitions, the double perovskite $Cs_2AgTlBr_6$ is deemed unsuitable for PV applications due to the toxicity of Tl^{3+}.[33]

Silver-bismuth iodide (Ag-Bi iodide) rudorffites are a family of fully inorganic bismuth halide semiconductors that were originally discovered as potential ionic conductors [34] and have recently attracted attention as PV absorber materials.[35–37] In contrast to low dimensional $A_3Bi_2I_9$, Ag-Bi iodides crystallize in a 3D network and, unlike the archetypical double perovskite $Cs_2AgBiBr_6$, retain strong absorption in the visible part of the spectrum.[36,38] Denoted by the general chemical formula $(AgI)_x(BiI_3)_y$ (or, alternatively, $Ag_xBi_yI_{x+3y}$), Ag-Bi iodides crystallize in the above-mentioned rudorffite crystal structure, building on an edge-sharing $[AgI_6]$ and $[BiI_6]$ octahedral network. Each cationic sublattice site can be understood as a joint, disordered population of monovalent Ag^+, trivalent Bi^{3+}, and neutral vacancy Δ, that is, the cation sublattice site is disorderedly occupied by Ag^+, Bi^{3+} or a vacancy (which refers to an empty sublattice site). Turkevych et al. describe the crystal structure of Ag-Bi iodides as alternating [M′X] and [M″X] layers where M′ and M″ are cationic lattice sites with differing combinations of population distribution ($M' = Ag_aBi_b\Delta_c$ and $M'' = Ag_{a'}Bi_{b'}\Delta_{c'}$).[39] An illustration of the crystal structure showing the disordered cation population is shown in **Figure 1**. The possible combinations of occupancies are constrained by stoichiometric and charge neutrality rules, thus restricting the number of phase-stable compositions. An in-depth discussion of the composition-dependent occupancies can be found in the Supporting Information. Among other compositions satisfying these constraints, four have been reported and studied across a range of literature reports mainly for photovoltaic applications: $AgBi_2I_7$, $AgBiI_4$, Ag_2BiI_5, and Ag_3BiI_6.[34,39–44]

Despite favorable optoelectronic properties including strong absorption in the visible range, long-range charge-carrier mobility values exceeding 1 $cm^2\ V^{-1}\ s^{-1}$ and lifetimes extending into the nanosecond timescale for Ag-Bi iodides,[44,45] the maximum PCE achieved by solar cells has to date been limited to ≈5.4%,[46] significantly lower than those attained by lead-halide perovskite-based devices. Such underperformance may be linked with an ultrafast charge-carrier localization process reported for a wide variety of Ag-Bi semiconductors including $Cs_2AgBiBr_6$,[32] $Cs_2AgSb_xBi_{1-x}Br_6$,[47] Cu_2AgBiI_6 [48], $AgBiS_2$ [49], and $Cu_{4x}(AgBi)_{1-x}I_4$ [50], thus raising profound questions on the potential of these materials for PV application. This charge-carrier localization process has been ascribed to the ultrafast formation of a "small polaron" state,[32,48] occurring within picoseconds after the original photoexcitation of a highly delocalized large polaron, which yields significantly reduced long-range mobilities. While Wu et al. pointed toward strong acoustic-phonon deformation potentials in Bi-based compounds and easily deformable Ag—halide bonds as the key contributors to charge-carrier localization in $Cs_2AgBiBr_6$,[51] Buizza et al. highlighted the importance of electronic dimensionality (i.e., the degree of overlap for band-edge orbitals) by examining the impact of increasing Cu^+ content in $Cu_{4x}(AgBi)_{1-x}I_4$ on the extent of charge-carrier localization.[50] However, intriguingly, not all bismuth halides exhibit such ultrafast charge-carrier localization: it has recently been shown that the bismuth halide derivative BiOI displays no such effects, despite lowered dimensionality and the presence of significant electron-phonon coupling.[52,53] Clearly, a deeper and more comprehensive understanding of the origin of charge-carrier localization in Bi-based semiconductors remains lacking and highly relevant. Crucially, it raises a question on the integrality of Ag-halide incorporation to the emergence of ultrafast charge-carrier localization in Ag-Bi semiconductors.

In this study, we investigate the charge-carrier dynamics in a series of thermally evaporated $(AgI)_x(BiI_3)_y$ thin films in order to elucidate the structure-property relationships that determine charge-carrier localization in Ag-Bi halide rudorffites. By using a combination of X-ray diffraction (XRD) and UV–vis absorption, we report a surprising invariance of the band gap in the $(AgI)_x(BiI_3)_y$ thin film series despite significant changes in the crystal structure. In contrast, extremely broad and monotonously shifting emission observed using photoluminescence (PL) spectroscopy is consistent with the presence of strong electron-phonon coupling and reveals the impact of varying Ag/Bi ratio on the excited state of charge carriers. Our conclusions are further validated by comparing the charge-carrier dynamics in the $(AgI)_x(BiI_3)_y$ thin film series using a combination of ultrafast THz-conductivity and transient absorption spectroscopy probes. We are thus able to independently trace the photoconductance and photoinduced charge-carrier population, thereby revealing the temporal evolution of charge-carrier mobility in these materials. We interpret the obtained results by correlating the structural vacancy incorporation in the $(AgI)_x(BiI_3)_y$

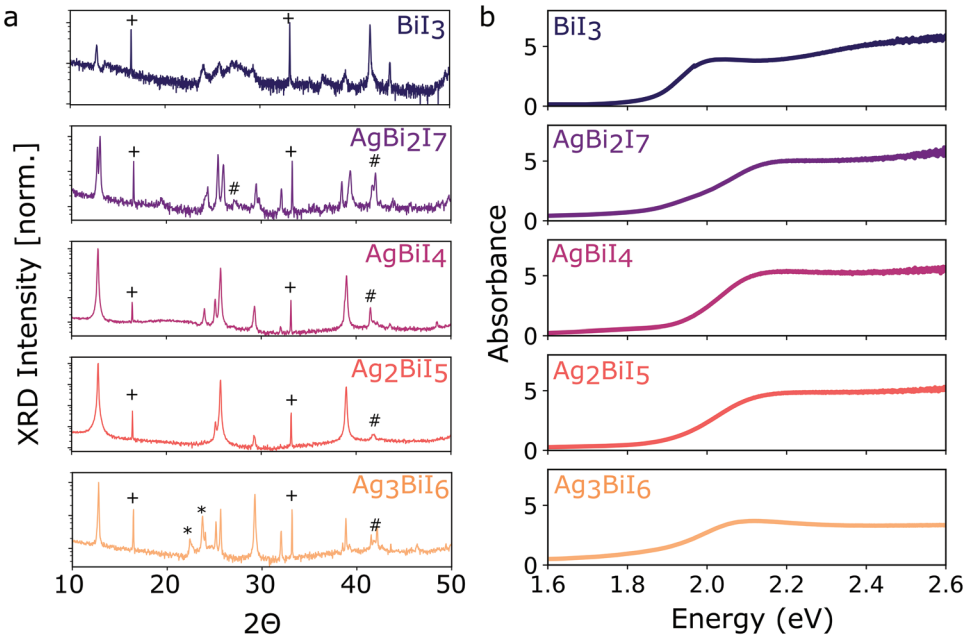

Figure 2. a) Experimental X-ray diffraction patterns of $(AgI)_x(BiI_3)_y$ thin films (see Figure S7, Supporting Information for the XRD pattern of AgI thin films) taken using Cu-Kα_1 as the radiation source. Impurity peaks belonging to BiI_3 and AgI are marked with (#) and (*) respectively. Reflections from the z-cut quartz substrate are marked with (+). b) Linear optical absorption spectra for the $(AgI)_x(BiI_3)_y$ thin films series, for compositions BiI_3, $AgBi_2I_7$, $AgBiI_4$, Ag_2BiI_5, and Ag_3BiI_6 measured by reflection-transmission spectroscopy. The y-axis corresponds to the absorbance of the thin films calculated as the product of the absorption coefficient (α) and thickness of the film.

crystal structure and the strength of charge-carrier localization, which we ascribe to vacancy-mediated lattice softening. Finally, through a comparison of alloyed ternary compositions (Ag-Bi iodides) with the binary precursor compositions (BiI_3 and AgI), we show that the presence of silver-halide bonds is extraneous to ultrafast charge-carrier localization. By examining the influence of alloying-mediated structural variation on charge-carrier dynamics in $(AgI)_x(BiI_3)_y$, our results address a key research gap and educate the strategy for future semiconductor design.

2. Results

$(AgI)_x(BiI_3)_y$ thin films used in this study were deposited on z-cut quartz substrates using dual-source co-evaporation of BiI_3 and AgI followed by thermal annealing. The obtained compositions are in good agreement with the nominal compositions of BiI_3, $AgBi_2I_7$, $AgBiI_4$, Ag_2BiI_5, and Ag_3BiI_6, as measured using scanning electron microscopy energy dispersive X-ray spectroscopy (SEM-EDX). Details of the fabrication procedure along with the exact composition of the thin films can be found in the Supporting Information.

2.1. Crystal Structure and Optical Absorption

To gain insight into the phases formed in the thin films, we carried out XRD measurements and performed phase identification and unit cell analysis by using the Pawley fitting method. The XRD patterns of BiI_3 and Ag-Bi iodide thin films are shown in **Figure 2a**; the corresponding Pawley fits for Ag-Bi iodide films can be found in Figure S1 (Supporting Information). The XRD pattern for the AgI thin film is shown in Figure S7 (Supporting Information). The fitting of the XRD pattern of Bi-rich $AgBi_2I_7$ revealed the co-existence of two ternary phases (trigonal and cubic) in the fabricated thin film, whereas only one ternary phase was obtained for the other Ag-Bi iodide compositions. Impurity peaks associated with BiI_3 were detected in all Ag-Bi iodide thin films with Ag-rich Ag_3BiI_6 thin film showing additional impurity peaks associated with AgI. As previously shown by Khazaee et al,[54] the gradual increase in Ag^+ content is accompanied by an increase in unit cell volume, derived largely from the progressive elongation of the *c*-axis (see Table S2, Supporting Information for unit cell parameters and phase information). This can be attributed to the incorporation of the larger ionic radius of Ag^+ compared to Bi^{3+} as the crystal structure transitions from the $CdCl_2$ octahedral motif in the $AgBi_2I_7$ and $AgBiI_4$ compounds to the $NaVO_2$ octahedral motif found in Ag_2BiI_5 and Ag_3BiI_6.[76] Figure S2 (Supporting Information) shows the top view scanning electron microscopy (SEM) images of the silver-bismuth iodide thin films. The grain sizes observed are of the order of hundreds of nanometers, in line with previous reports.[35,38,55]

Figure 2b shows the linear absorption spectra for BiI_3 and the four Ag-Bi iodide compositions with the absorbance representing the product of the absorption coefficient and the thickness of the film. All measured compositions show a broad onset of the absorbance at ∽1.8 eV, in line with previously reported spectra.[36,39,44] We note that in the presence of such a broadened onset, the estimated band gap is highly dependent on the method used to analyze the absorption onset. Tauc's method has been widely used to extract band gaps for these materials, with values

between 1.73 and 1.85 eV reported under the assumption of a direct band gap, and slightly lower values of 1.6–1.73 eV following the assumption of an indirect band gap.[36,43,44] However, the possible presence of excitonic contributions to the absorption spectrum, and the high degree of disorder and high defect density can cause underestimated band gap values to be extracted from Tauc's method.[56] In contrast, we adopt Elliott's method here to determine a band gap and decouple the excitonic and free charge-carrier contribution. A detailed explanation of the fitting regimen along with the extracted parameters (Table S3, Supporting Information) and obtained fits (Figure S4, Supporting Information) can be found in Supporting Information. From these Elliott fits, we obtain a relatively unchanged band gap across the compositions, lying between 1.96 and 2.15 eV. We note that the values extracted here are lower than those reported by Ghosh et al. and slightly higher than those reported in a previous work by Buizza et al. for $AgBiI_4$.[44,50]

It is interesting to note that the shape of the absorption curve does not vary significantly with the composition. Sansom et al. previously interpreted this through DFT-based projected density-of-states (PDOS) calculations and suggested that band-edge states in Ag-Bi iodides closely resemble those of BiI_3, thus providing a robust explanation for the compositional invariance of the band gap.[36] Alternatively, it has been suggested for Ag-Bi double perovskites that weak electronic coupling between $[AgI_6]$ and $[BiI_6]$ octahedra leads to a quasi-0D electronic structure close to the band edge.[57] In such a scenario, altering the Ag/Bi content is not likely to meaningfully shift the energetic levels of the orbitals contributing to the band edge states for alloyed compositions. All compositions exhibit a respectable absorbance of ≈5 measured at 530 nm which, for the given film thicknesses of 250–300 nm, yields absorption coefficients of $\approx 10^5$ cm^{-1} in line with previous reports.[35,36] Given the strengths of absorption coefficients, these onsets and extracted bandgaps are clearly associated with direct optically-allowed transitions, however, we note that this does not preclude the presence of indirect gaps below the direct onsets investigated here.

2.2. Ultrafast Charge-Carrier Localization

The invariability of the bandgap across the $(AgI)_x(BiI_3)_y$ thin film series raises important questions about the impact of changing composition on the charge-carrier dynamics in the materials. Though the presence of ultrafast charge-carrier localization in $AgBiI_4$ has been previously reported by Buizza et al.,[50] it has not yet been explored for the other compositions studied in this work. Therefore, we first examine the ultrafast charge-carrier dynamics in the $(AgI)_x(BiI_3)_y$ thin-film series by measuring photoinduced THz conductivity transients using optical-pump terahertz-probe spectroscopy (OPTPS). As discussed previously by Wright and Buizza et al.,[32,48] ultrafast localization (over a timescale of ≈1 ps) of charge carriers radically changes the transport regime. While immediately upon photoexcitation, charge carriers exhibit bandlike transport, after the localization process, they diffuse through the material using a thermally-activated hopping mechanism. Such hopping transport associated with the presence of energy barriers leads to significantly reduced charge-carrier mobility, making OPTPS uniquely positioned to capture the localization process by measurement of the THz photoconductivity with picosecond time resolution.

Figure 3a shows the normalized OPTPS transients for the $(AgI)_x(BiI_3)_y$ thin-film series, measured following excitation with 2.34 eV photons. It is important to note that at this excitation energy, we do not inject charge carriers into any AgI impurities that may inadvertently have been included, because AgI has a band gap larger than 2.7 eV as seen from the absorption spectrum shown in Figure S8 (Supporting Information). Notably, OPTPS transients for all Ag-Bi iodides and BiI_3 show similar behavior: an ultrafast photoconductivity decay within the first 2 picoseconds, which has previously been shown to be a fingerprint of a charge-carrier localization process.[32,48,58,59] While in principle other mechanisms can cause a rapid decay of the photoconductivity (e.g., exciton formation, higher-order recombination), we note that the lack of fluence dependence for this ultrafast decay (see below and Figure S9, Supporting Information) and its persistence at low pump fluences (< 20 μJ cm^{-2}) rules out such possible contributions from higher-order effects. We further prove that the observed ultrafast photoconductivity decay does not result from monomolecular charge-carrier recombination, e.g. mediated by traps, by measuring the dynamics of the photoinduced charge-carrier density by ultrafast transient absorption (TA) for all the compositions in the $(AgI)_x(BiI_3)_y$ thin film series. For every composition, the TA trace measured at 1.9 eV (shown in Figure 3b) following a 2.34 eV excitation pulse corresponds to photoinduced absorption (PIA), in agreement with previously reported TA spectra reported for Ag-Bi iodides,[40] which show a broad, featureless PIA band ranging from 1.8 to 2.1 eV. Given the immediate, sub-picosecond rise after photoexcitation observed for the PIA, this signal can safely be interpreted as a signature of the photoexcited charge-carrier density in the material. The TA kinetics can be adequately described using a phenomenological biexponential decay model as seen from the fits to the data (solid lines) with an initial ultrafast decay ($1/k_{loc}$, τ_{loc} ≈1 ps) followed by a slow decay ($1/k_1$, τ_1 > 100 ps for Ag-Bi iodides). The slow decay in case of BiI_3 is extremely slow and therefore the time constant cannot be accurately resolved from the measured TA trace. The extracted fit parameters are summarized in Table S4 (Supporting Information). The ultrafast decay in PIA kinetics is in agreement with previous studies on silver-bismuth halides and BiI_3 and has previously been attributed to charge-carrier cooling caused by scattering with phonons.[40,60] Crucially, the presence of a substantial long-lived TA component revealed by the long τ_2 observed for all the thin films studied is strongly indicative of a persistent charge-carrier population in these materials. While the TA signal is proportional to the photoinduced charge-carrier population $\Delta A \propto n$, the OPTP signal is proportional to its product with the electron-hole sum mobility $\Delta T/T \propto n\mu$. Consequently, the drop in photoconductance observed in the OPTPS traces cannot be solely ascribed to charge-carrier recombination (i.e., ultrafast decay in n). Rather, the ultrafast decay observed in OPTP reflects a reduction in charge-carrier mobility in the system, supporting the presence of charge-carrier localization.

We further explore whether charge-carrier trapping at extrinsic defects could alternatively be the cause of localization as it could theoretically also explain the concurrent long-lived TA and diminished photoconductance. To resolve this question, we measure OPTP transients at different excitation fluences (Figure S9,

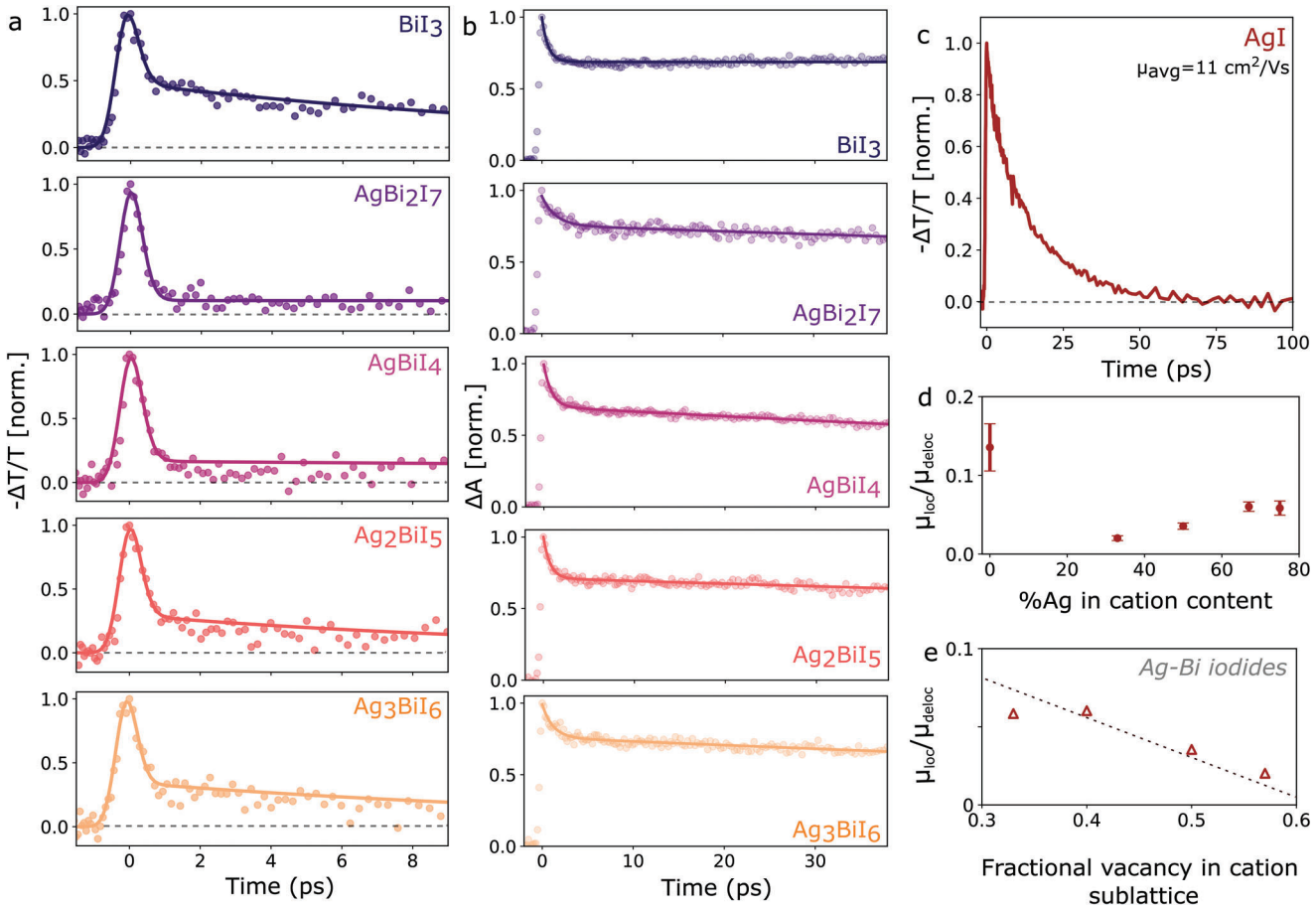

Figure 3. a) Normalized photoinduced THz conductivity transients measured for $(AgI)_x(BiI_3)_y$ thin films with nominal compositions BiI_3, $AgBi_2I_7$, $AgBiI_4$, Ag_2BiI_5, and Ag_3BiI_6 after 2.34 eV pulsed excitation. The colored circles show the experimental data while the solid lines in the same color represent fits based on the two-level mobility model described in Supporting Information b) Normalized transient absorption traces for thin films with nominal compositions BiI_3, $AgBi_2I_7$, $AgBiI_4$, Ag_2BiI_5, and Ag_3BiI_6 measured after 2.34 eV pulsed excitation and detected at a probe energy of 1.9 eV. The colored circles show the experimental data while the solid lines in the same color represent phenomenological bi-exponential fits to the data c) Normalized THz-photoconductivity transient measured for an AgI thin film following 3.1 eV excitation. d) Fractional retained electron-hole sum mobility (μ_{loc}/μ_{deloc}) plotted as a function of percentage Ag content in the composition calculated as $\frac{N_{Ag}}{N_{Bi}+N_{Ag}} \times 100$. e) The fractional retained charge-carrier mobility (μ_{loc}/μ_{deloc}) in Ag-Bi iodides plotted against the fractional vacancy incorporation in the cationic sublattice. The relation between composition and the fraction of vacancies in the cationic sublattice is explained in Supporting Information. The dotted line is a guide for the eye.

Supporting Information) which show a distinct lack of fluence dependence even toward high incident fluences (≈40 μJ cm^{-2} corresponding to a photoexcited charge-carrier density larger than 10^{18} cm^{-3}) highlighting a lack of trap saturation behavior. Considering the moderate defect concentrations (≤ 10^{17} cm^{-3}) and capture cross-section (≈10^{-19} cm^2) reported for such materials in previous works by Pecunia et al. and Wu et al.,[45,61] we therefore conclude that the localization phenomenon is intrinsic in nature. Thus, our observations strongly validate the presence of intrinsic charge-carrier self-localization across all Ag-Bi iodides and BiI_3. Notably, the discovery of persistent charge-carrier localization, even in BiI_3, demonstrates that the presence of silver-halide bonds alone is not the main cause driving charge-carrier localization in Bi-halide derivatives.

OPTP transients measured for AgI following 3.1 eV excitation (shown in Figure 3c) show a complete absence of any ultrafast localization process in line with the results of previous investigations into the charge-carrier dynamics of silver halides.[62] We note that the absence of self-trapping in AgI supports our conclusions on the insignificance of silver-halide bonds to the presence of charge-carrier localization discussed above. However, given the significantly different crystal and band structures of AgI compared to BiI_3 and mixed Ag-Bi iodides (both of which are expected to substantially impact the optoelectronic properties of a material),[63,64] we refrain from deriving conclusions by directly comparing the charge-carrier dynamics of AgI to those observed for BiI_3 and mixed Ag-Bi iodides.

Having conclusively established the presence of ultrafast charge-carrier localization in both Ag-Bi iodides and BiI_3, we move on to investigate the electronic transport properties of these materials. From the measured OPTP transients, we extract the effective electron-hole sum mobilities using the initial photoconductivity value (proportional to -Δ*T*/*T*) and the

calculated density of photoexcited charge carriers immediately following photoexcitation. At this point in time, generated photocarriers exist in their initial fully delocalized state, and therefore the extracted mobility reflects that of the delocalized state (μ_{deloc}), that is, the large polaron prior to self-localization. A detailed description of the mobilities extraction procedure is provided in the Supporting Information. As shown in Figure S10 (Supporting Information), BiI_3 exhibits the highest value for the initial delocalized-state mobility, with $\mu_{deloc} \approx 1.4$ cm^2 Vs^{-1}, whereas Ag-Bi halides exhibit a considerably lower μ_{deloc} of ≈ 0.5 cm^2 Vs^{-1}. Given that the band edge mobility of charge carriers is generally a function of the band curvature through its relationship with their effective mass ($m_{eff} \propto [d^2E/dk^2]^{-1}$),[65] this trend is in line with expectations based on band structure calculations reported by Sansom et al.[50] which show a more pronounced band curvature in case of BiI_3 compared with flatter band edge states for $AgBiI_4$.[36] Interestingly, μ_{deloc} does not change significantly with composition within the Ag-Bi iodide series revealing that changing ratios of Ag/Bi content in the material indeed does not significantly influence the band-edge states.

We further examine the extent to which charge carriers lose mobility as a result of the ultrafast localization process. Such relative mobility reduction is visually apparent from the photoconductivity transients displayed in Figure 3a by comparison of the conductivities attained initially and soon after the localization process has been completed. However, to obtain more quantitative values, we fit the OPTP transients of $(AgI)_x(BiI_3)_y$ thin films with a two-level mobility model developed by Wright and Buizza et al. to capture such localization processes for a range of Ag-Bi semiconductors.[32,48] The details of the model along with the extracted parameters are provided in the Supporting Information (Table S5). The derived fits are plotted as solid lines in Figure 3a, which show good agreement with the experimental data (colored markers). We extract values for mobility μ_{loc} of the localized state in addition to other parameters such as rate of localization (k_{loc}) and rate of relaxation (k_1). Using the delocalized mobility determined earlier, we calculate the ratio of the two mobilities, $R = \mu_{loc}/\mu_{deloc}$, plotted in Figure 3d in order to evaluate the trend in strength of charge-carrier localization. We consider the value of R as the meaningful parameter here, because, while μ_{loc} depends strongly on the extent of localization,[66,67] it may also depend on extrinsic factors such as crystallinity and the presence of ionized defects, and intrinsic factors such as changes in band structure. We therefore divide μ_{loc} by the value of μ_{deloc}, assuming this as a baseline that may reflect trends resulting from such effects. Interestingly, Figure 3d reveals that R shows the greatest magnitude for BiI_3 ($R \approx 0.13$), indicating the highest mobility retention and therefore lowest localization effects, and drops sharply with small amounts of silver inclusion ($R \approx 0.02$ for $AgBi_2I_7$). Within the alloyed silver-bismuth iodide series, R slightly increases for compositions with higher silver content ($R \approx 0.06$ for Ag_3BiI_6) indicating a small recovery in mobility retention. Overall, the fractional retained mobilities in $(AgI)_x(BiI_3)_y$ compositions considered in this study are much lower than those reported for $Cs_2AgBiBr_6$ ($R \approx 0.3$),[32] Cu_2AgBiI_6 ($R \approx 0.45$) [48], and $AgBiS_2$ ($R \approx 0.8$),[49] showing that $(AgI)_x(BiI_3)_y$ rudorffites are particularly prone to such self-localization effects.

2.3. Broadband Photoluminescence

While charge-carrier localization is known to be detrimental for photovoltaic applications, broadband luminescence from self-trapped exciton (or small polaron) states is considered promising for white light generation.[68] Thus, having confirmed the presence of charge-carrier localization in $(AgI)_x(BiI_3)_y$ thin films, we continue by studying the photoluminescence properties of these materials. **Figure** 4a–e reveals that all measured compositions exhibit extremely broad PL (with FWHM ≈ 0.5 eV for Ag-Bi iodides and FWHM ≈ 0.3 eV for BiI_3) stretching into the infrared. We note that correctly measuring such broad PL is a challenging task, since the spectra extend far beyond the range that can be detected by the widely used silicon CCD detectors. We note that previously reported PL spectra for Ag-Bi iodides have shown a PL extending only to ≈ 1100 nm [35,39], which corresponds to the typical Si-CCD detector response cut-off associated with the bandgap of silicon. In contrast, we were able to reveal the complete PL spectrum here by extending detectivity further into the IR, using both a Si-CCD and an InGaAs (IGA) detector and combining the spectra. The experimental procedure for measuring the PL along with a detailed explanation of the data analysis is provided in the Supporting Information.

A broad PL linewidth has previously been reported for a range of semiconductors showing strong electron-phonon coupling.[32,48,52] A comparison with the absorption spectra also reveals a large Stokes shift of several hundred meV between the direct bandgaps determined from the strong absorption onsets above, and the detected PL peak energies. Thus, the observed PL is unlikely to derive from direct band-to-band transitions which in itself is not surprising given that these materials are widely accepted to be indirect bandgap materials.[37,38] Furthermore, given that first principles calculations have pinned the difference between the direct and the indirect band gap to ≈ 0.1 eV,[36,38] we can preclude any contribution to the PL (in case of Ag-Bi iodides) from direct radiative recombination across the indirect band gap. Therefore, while a number of causes can give rise to such a broad and Stokes-shifted PL (including inhomogeneous broadening from disorder, strongly lattice coupled defect PL and the formation of a self-trapped exciton) [48,69–71], based on our observations of ultrafast charge-carrier localization discussed above, we attribute such broad, redshifted PL to emission from the self-localized state.

Interestingly, the observed PL for all compositions deviates from a simple single lineshape function, and instead displays a number of features suggesting the presence of multiple, poorly-resolved PL peaks. We posit that multiple radiative pathways exist in Ag-Bi iodides, possibly originating from multiple energetically diverse localized states and/or strongly lattice-coupled defect states in the material. Thus, we fit the PL lineshape for all the studied thin films with a sum of Lorentzian peak functions, to resolve the individual peaks. We note that while there is limited utility of a multi-peak analysis in the absence of more information about the number of peaks and dominant defect energies, it may be cautiously used to analyze broad trends in PL across the series. We find that three Lorentzian peaks are necessary to describe the measured data for the alloyed series, with the exception of BiI_3, for which just two Lorentzian peaks are sufficient to describe the PL (as shown in Figure 4a–e). For the Ag-Bi iodide

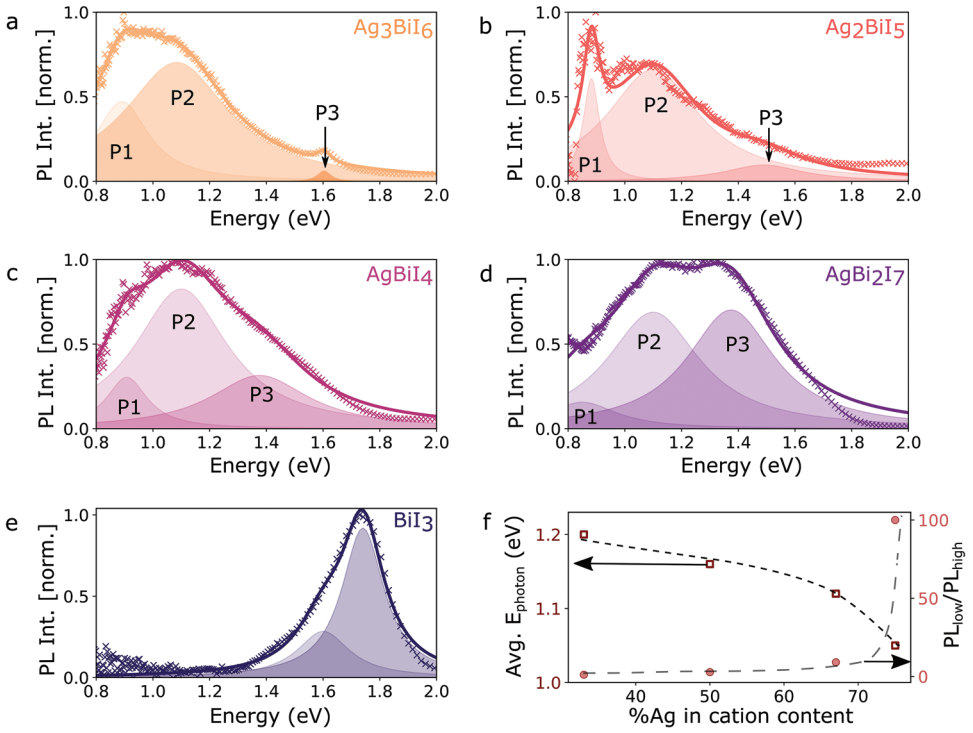

Figure 4. a–e) Photoluminescence (PL) spectra for $(AgI)_x(BiI_3)_y$ thin films with varying compositions measured following 532 nm continuous wave excitation. The measured PL was detected using a cooled Si-CCD in the high-energy range (600–1100 nm) and a cooled InGaAs detector in the low-energy range (950–1600 nm). The experimental data shown by colored cross markers was obtained by combining the PL measured on both detectors through stitching based on a protocol described in Supporting Information. The PL was fit with a sum of several Lorentzian functions shown in the colored solid line with the individual Lorentzians plotted as shaded area curves. f) Composition-dependent variation in PL_{low}/PL_{high} (round markers, right axis) calculated as the ratio of the high-energy contribution (area under peak P_3) and the low-energy contribution (sum of areas under the peaks P_1 and P_2). Composition-dependent average photon energy E_{photon} (square markers, left axis) calculated as the intensity weighted average of the photon emission energy ($= \sum N_\lambda E_\lambda / \sum N_\lambda$, where N_λ is the number of detected photons with energy lying within an interval of width ΔE centered at E_λ which corresponds to the PL intensity measured at E_λ). Dashed lines are guides to the eye.

emission spectra we thus label the peaks P1, P2, and P3 going from low to high photon energy.

While the observed PL trends might qualitatively suggest that increasing the Ag content in the composition leads to a larger red shift in the PL, our Lorentzian fits interpret this red shift as a result of the relative suppression of the high-energy peak P_3 in compositions with higher fractional Ag content. As shown in Figure 4f, such hypothesis is further supported by the calculated ratio P_{low}/P_{high} of the area under the low-energy emission peaks (P_1 and P_2) and the area under high-energy emission peak (P_3) plotted against the percentage of Ag content in the total cationic (Ag and Bi) presence, calculated as $100\times N_{Ag}/(N_{Ag}+N_{Bi})$. The figure clearly indicates an increasing trend in P_{low}/P_{high} with increasing Ag fraction in the overall cation content. We note that the trend does not depend on the arbitrary choice of high- and low-energy peaks. We observe the same effect through an alternative metric, that is, by calculating the average energy of emitted PL photons, E_{photon}, which is also plotted against the Ag content in Figure 4f, where $E_{photon} = \sum N_i E_i / \sum N_i$, and N_i is the number of detected photons with energy lying between E_i and $E_i+\Delta E$. The average emission energy E_{photon} decreases from 1.2 eV for $AgBi_2I_7$ to ≈1 eV for Ag_3BiI_6 with increasing Ag content, compatible with the suppression of high energy emission.

It has previously been suggested that, owing to their lower charge-carrier mobility, localized charge carriers cannot efficiently sample the full energetic landscape in a material, thus causing a violation of the Kasha–Vavilov principle (which states that the emission always originates from the lower energy state).[62] In the presence of multiple, spatially-separated emitting centers, such limitation of charge-carrier motion can lead to competing emissions from a range of low- and high-energy states, with relative intensities depending on the strength of the charge-carrier localization (i.e., on the mobility of the localized state). According to this interpretation, the lowering of PL emission energies with increasing Ag fraction may thus be associated with weaker charge-carrier localization allowing for more efficient charge-carrier exploration of the energetic landscape and funneling into lower-energy states. Resolving the exact nature of these luminescent states requires in-depth knowledge about the energetic levels of self-trapped and defect states in the system, which are currently still debated in literature. Previous experimental investigations into the defect levels in Ag_3BiI_6 by Merker et al. revealed the presence of deep traps 0.6 eV away from the band edge.[40] On the other hand, Pecunia et al. used photoinduced current transient spectroscopy (PICTS) to identify two defect levels with energetic depths of 0.25 and 0.33 eV relative to the relevant band edges.[61] It is likely that a range of luminescent

defects of different levels could be present, with different energetic offsets compared to the band edges, which would contribute to the observed broad-ranging PL. More detailed investigations into the levels of the self-trapped states contributing to the broad luminescence would thus be an interesting subject of future study.

The measured PL spectrum for BiI_3 corresponds well to previously reported spectra for the material.[35,72] The observed emission for BiI_3 is blue-shifted and narrower compared to those measured for Ag-Bi iodides, suggesting the presence of weaker electron-phonon coupling in BiI_3. Notably, for BiI_3, we do not observe the low-energy PL peaks exhibited by the alloyed Ag-Bi iodides, though we suspect that in this case the absence of it is more likely to be associated with different chemistry or defect density and does not exclusively depend on the strength of charge-carrier localization in the material.

3. Discussion

Taken together, our results show clear trends in self-localization of charge carriers across the series of $(AgI)_x(BiI_3)_y$ semiconductors, manifested by ultrafast, picosecond loss in conductivity and broad, redshifted photoluminescence. We thus proceed to discuss the mechanisms underlying such localization processes in $(AgI)_x(BiI_3)_y$. The endpoints of the series, BiI_3 and AgI show the lowest degrees of charge-carrier localization, with AgI exhibiting none, and BiI_3 a small degree of localization. However, for the mixed Ag-Bi compositions, $(AgI)_x(BiI_3)_y$ rudorffites exhibit relatively severe localization, with mobility retention factors increasing with increases in silver content. We discuss below three factors that are likely to contribute to these trends, that is, the fraction of vacancies in the cationic sublattice, changes in electronic dimensionality, and cation disorder.

First, we discuss the role of vacancies in the cationic sublattice in the trends in self-localization observed across the mixed Ag-Bi iodide series. As discussed previously, such vacancies (which refer to empty cationic sublattice sites) are incorporated within a perfect crystal structure of BiI_3 and Ag-Bi iodides in order to satisfy charge-balance constraints and are different from vacancy defects which generally arise from the loss of an ion from its original lattice site. In Figure 3e, we plot across the mixed Ag-Bi compositions the mobility retention factor R as a function of the fraction of vacancies in the cationic sublattice (see Supporting Information for details of determination). We find that higher fractions of vacancies in the crystal structure are correlated with stronger self-localization of charge carriers (i.e., with a smaller mobility retention). While there are no literature reports about the correlation between charge-carrier localization and vacancies in the crystal to the best of our knowledge, we interpret this correlation in terms of the structural effect of lattice vacancies. As already discussed, short-range interactions such as the acoustic deformation potential are essential to the formation of small polaron states in semiconductors.[73] Past studies have shown a link between lattice softness and vacancies, such as in the work by Tan et al. where Sn vacancies were found to lead to an enhancement in lattice softening in SnTe-$AgSbTe_2$ alloys.[74] Therefore, we posit that the presence of lattice vacancies yields more deformable crystal structures, and that such effects may lead to stronger polaronic effects and charge-carrier localization.

In order to explain the weaker localization in the end point composition BiI_3 compared to the alloyed $(AgI)_x(BiI_3)_y$, we further note that the electronic dimensionality of the material has a significant impact on charge-carrier localization in a material. While Ag-Bi iodides crystallize in a 3D structural network, by transferring the VBM onto Ag-4d orbitals while the CBM remains on the Bi-6p orbitals,[37] the addition of silver likely leads to a pseudo-zero electronic dimensionality in these materials as has been previously proposed for Ag-Bi double perovskites.[57] In contrast, BiI_3 exhibits a 2D structural network and therefore most likely an electronic dimensionality larger than one. Therefore, we suggest that the steep enhancement in the strength of localization on going from BiI_3 to mixed Ag-Bi iodides is a function of a sudden change in electronic dimensionality.

An additional reason why self-localization of charge carriers is much more severe in the mixed Ag-Bi compositions $(AgI)_x(BiI_3)_y$ than for BiI_3 may be found in cation disorder that is only found in the alloys. By moving from binary to ternary compositions, Ag-Bi alloying introduces an added parameter of cation disorder which may have a clear effect on charge-carrier transport in $(AgI)_x(BiI_3)_y$. The impact of cation disorder has been studied in other disordered materials such as kesterites (CZTS), where the formation of localized states mediated by cation segregation was found to detrimentally impact charge-carrier transport.[75] Recently, Righetto et al. examined the impact of cation disorder on the charge-carrier localization in $AgBiS_2$.[49] Here, the formation of segregated Ag-rich and Bi-rich domains was found to cause stronger charge-carrier localization as a result of a more disordered energetic landscape to which small polarons are particularly susceptible. We, therefore, propose that cation disorder may also lead to similar charge-carrier transport inhibition in the alloyed Ag-Bi iodides investigated here, thus explaining the stronger charge-carrier localization observed in ternary compositions as compared to their binary endpoints.

4. Conclusion

In this work, we have examined the optoelectronic properties of $(AgI)_x(BiI_3)_y$ thin films to elucidate the impact of changing Ag/Bi ratios on the charge-carrier dynamics and emissive properties of these semiconductors. We used a combination of steady-state (UV–vis absorption and PL) and transient (OPTP and TA) spectroscopic techniques to investigate trends with changing chemical composition. Observing invariant absorption onsets and charge-carrier mobility of the initially formed delocalized state, we conclude that varying the Ag/Bi has little impact on the electronic structure near the band edge. This observation is surprising, given the compositionally varying crystal structure, and we interpret it as a verification of the previously suspected low electronic dimensionality of Ag-Bi iodides. Our transient spectroscopic measurements reveal the presence of ultrafast charge-carrier localization in both BiI_3 and Ag-Bi iodides on a picosecond time scale. By thus demonstrating that the presence of Ag^+ cations is not necessary to the emergence of a localization process in Bi-based PIMs, we show that these effects cannot be simply attributed to soft silver-halide bonds alone. However, our findings reveal that mixed Ag-Bi iodides do exhibit stronger charge-carrier localization compared to the endpoint BiI_3, which we attribute to a combination of reduced electronic dimensionality and

enhanced cation disorder. Within the Ag-Bi iodide series, the impact of reducing silver content manifests as an increase in structurally incorporated vacancies that leads to stronger charge-carrier localization, which we attribute to enhancements in vacancy-mediated lattice softening. Overall, our study addresses a gap in understanding the structure-property relationships that fundamentally impact the charge-carrier dynamics of $(AgI)_x(BiI_3)_y$ and lays a foundation for the design of Bi-based PIMs with enhanced performance.

Supporting Information

Supporting Information is available from the Wiley Online Library or from the author.

Conflict of Interest

H.J.S. is co-founder and CSO of Oxford PV Ltd.

Data Availability Statement

The data that support the findings of this study are available from the corresponding author upon reasonable request.

Keywords

charge-carrier dynamics, mobility, silver-bismuth halides, solar cells, thin films

Received: December 13, 2023
Revised: March 24, 2024
Published online:

[1] M. A. Green, E. D. Dunlop, M. Yoshita, N. Kopidakis, K. Bothe, G. Siefer, X. Hao, *Prog. Photovolt Res. Appl.* **2023**, *31*, 3.
[2] Photovoltaic Research, Best Research-Cell Efficiency Chart, NREL, Golden, CO (accessed: October 2023).
[3] H. Min, D. Y. Lee, J. Kim, G. Kim, K. S. Lee, J. Kim, M. J. Paik, Y. K. Kim, K. S. Kim, M. G. Kim, T. J. Shin, S. Il Seok, *Nature.* **2021**, *598*, 444.
[4] J. Park, J. Kim, H. S. Yun, M. J. Paik, E. Noh, H. J. Mun, M. G. Kim, T. J. Shin, S. Il Seok, *Nature.* **2023**, *616*, 724.
[5] H. Li, W. Zhang, *Chem. Rev.* **2020**, *120*, 9835.
[6] K. Xiao, R. Lin, Q. Han, Y. Hou, Z. Qin, H. T. Nguyen, J. Wen, M. Wei, V. Yeddu, M. I. Saidaminov, Y. Gao, X. Luo, Y. Wang, H. Gao, C. Zhang, J. Xu, J. Zhu, E. H. Sargent, H. Tan, *Nat. Energy.* **2020**, *5*, 870.
[7] L. Li, Y. Wang, X. Wang, R. Lin, X. Luo, Z. Liu, K. Zhou, S. Xiong, Q. Bao, G. Chen, Y. Tian, Y. Deng, K. Xiao, J. Wu, M. I. Saidaminov, H. Lin, C. Q. Ma, Z. Zhao, Y. Wu, L. Zhang, H. Tan, *Nat. Energy.* **2022**, *7*, 708.
[8] T. Leijtens, K. A. Bush, R. Prasanna, M. D. McGehee, *Nat. Energy.* **2018**, *3*, 828.
[9] G. E. Eperon, T. Leijtens, K. A. Bush, R. Prasanna, T. Green, J. T.-W. Wang, D. P. McMeekin, G. Volonakis, R. L. Milot, R. May, A. Palmstrom, D. J. Slotcavage, R. A. Belisle, J. B. Patel, E. S. Parrott, R. J. Sutton, W. Ma, F. Moghadam, B. Conings, A. Babayigit, H.-G. Boyen, S. Bent, F. Giustino, L. M. Herz, M. B. Johnston, M. D. McGehee, H. J. Snaith, *Science.* **2016**, *354*, 861.
[10] C. C. Boyd, R. Cheacharoen, T. Leijtens, M. D. McGehee, *Chem. Rev.* **2019**, *119*, 3418.
[11] T. Leijtens, G. E. Eperon, N. K. Noel, S. N. Habisreutinger, A. Petrozza, H. J. Snaith, *Adv. Energy Mater.* **2015**, *5*, 1500963.
[12] T. Miyasaka, A. Kulkarni, G. M. Kim, S. Öz, A. K. Jena, *Adv. Energy Mater.* **2020**, *10*, 1902500.
[13] M. Chen, M. G. Ju, H. F. Garces, A. D. Carl, L. K. Ono, Z. Hawash, Y. Zhang, T. Shen, Y. Qi, R. L. Grimm, D. Pacifici, X. C. Zeng, Y. Zhou, N. P. Padture, *Nat. Commun.* **2019**, *10*, 16.
[14] A. Marronnier, G. Roma, S. Boyer-Richard, L. Pedesseau, J. M. Jancu, Y. Bonnassieux, C. Katan, C. C. Stoumpos, M. G. Kanatzidis, J. Even, *ACS Nano.* **2018**, *12*, 3477.
[15] W. Li, J. Li, J. Li, J. Fan, Y. Mai, L. Wang, *J Mater Chem A Mater.* **2016**, *4*, 17104.
[16] N. K. Noel, S. D. Stranks, A. Abate, C. Wehrenfennig, S. Guarnera, A. A. Haghighirad, A. Sadhanala, G. E. Eperon, S. K. Pathak, M. B. Johnston, A. Petrozza, L. M. Herz, H. J. Snaith, *Energy Environ. Sci.* **2014**, *7*, 3061.
[17] Y. Peng, T. N. Huq, J. Mei, L. Portilla, R. A. Jagt, L. G. Occhipinti, J. L. MacManus-Driscoll, R. L. Z. Hoye, V. Pecunia, *Adv. Energy Mater.* **2021**, *11*, 2002761.
[18] N. Glück, T. Bein, *Energy Environ. Sci.* **2020**, *13*, 4691.
[19] W. Ke, M. G. Kanatzidis, *Nat. Commun.* **2019**, *10*, 965.
[20] W.-J. Yin, T. Shi, Y. Yan, *Adv. Mater.* **2014**, *26*, 4653.
[21] F. Ünlü, M. Deo, S. Mathur, T. Kirchartz, A. Kulkarni, *J Phys D Appl Phys.* **2022**, *55*, 113002.
[22] R. E. Brandt, V. Stevanović, D. S. Ginley, T. Buonassisi, *MRS Commun.* **2015**, *5*, 265.
[23] A. Walsh, A. Zunger, *Nat. Mater.* **2017**, *16*, 964.
[24] A. J. Lehner, D. H. Fabini, H. A. Evans, C. A. Hébert, S. R. Smock, J. Hu, H. Wang, J. W. Zwanziger, M. L. Chabinyc, R. Seshadri, *Chem. Mater.* **2015**, *27*, 7137.
[25] X. Chen, M. Jia, W. Xu, G. Pan, J. Zhu, Y. Tian, D. Wu, X. Li, Z. Shi, *Adv. Opt. Mater.* **2023**, *11*, 2202153.
[26] X. Wang, T. Li, B. Xing, M. Faizan, K. Biswas, L. Zhang, *J. Phys. Chem. Lett.* **2021**, *12*, 10532.
[27] B. Ghosh, S. Chakraborty, H. Wei, C. Guet, S. Li, S. Mhaisalkar, N. Mathews, *J. Phys. Chem. C.* **2017**, *121*, 17062.
[28] F. Ji, J. Klarbring, F. Wang, W. Ning, L. Wang, C. Yin, J. S. M. Figueroa, C. K. Christensen, M. Etter, T. Ederth, L. Sun, S. I. Simak, I. A. Abrikosov, F. Gao, *Angew Chem Int Ed.* **2020**, *59*, 15191.
[29] C. Wu, Q. Zhang, Y. Liu, W. Luo, X. Guo, Z. Huang, H. Ting, W. Sun, X. Zhong, S. Wei, S. Wang, Z. Chen, L. Xiao, *Adv. Sci.* **2018**, *5*, 1700759.
[30] M. Delor, A. H. Slavney, N. R. Wolf, M. R. Filip, J. B. Neaton, H. I. Karunadasa, N. S. Ginsberg, *ACS Energy Lett.* **2020**, *5*, 1337.
[31] A. H. Slavney, T. Hu, A. M. Lindenberg, H. I. Karunadasa, *J. Am. Chem. Soc.* **2016**, *138*, 2138.
[32] A. D. Wright, L. R. V. Buizza, K. J. Savill, G. Longo, H. J. Snaith, M. B. Johnston, L. M. Herz, *J. Phys. Chem. Lett.* **2021**, *12*, 3352.
[33] A. H. Slavney, L. Leppert, A. Saldivar Valdes, D. Bartesaghi, T. J. Savenije, J. B. Neaton, H. I. Karunadasa, *Angew. Chem.* **2018**, *130*, 12947.
[34] L. F. Mashadieva, Z. S. Aliev, A. V. Shevelkov, M. B. Babanly, *J. Alloys Compd.* **2013**, *551*, 512.
[35] A. Crovetto, A. Hajijafarassar, O. Hansen, B. Seger, I. Chorkendorff, P. C. K. Vesborg, *Chem. Mater.* **2020**, *32*, 3385.
[36] H. C. Sansom, G. F. S. Whitehead, M. S. Dyer, M. Zanella, T. D. Manning, M. J. Pitcher, T. J. Whittles, V. R. Dhanak, J. Alaria, J. B. Claridge, M. J. Rosseinsky, *Chem. Mater.* **2017**, *29*, 1538.
[37] H. Wu, H. Zhu, A. Erbing, M. B. Johansson, S. Mukherjee, G. J. Man, H. Rensmo, M. Odelius, E. M. J. Johansson, *ACS Appl. Energy Mater.* **2019**, *2*, 5356.

[38] H. Zhu, A. Erbing, H. Wu, G. J. Man, S. Mukherjee, C. Kamal, M. B. Johansson, H. Rensmo, M. Odelius, E. M. J. Johansson, *ACS Appl. Energy Mater.* **2020**, *3*, 7372.
[39] I. Turkevych, *ChemSusChem.* **2017**, *10*, 3754.
[40] A. Merker, M. Morgenroth, M. Scholz, T. Lenzer, K. Oum, *J. Phys. Chem. C.* **2022**, *127*, 1487.
[41] Y. Seo, S. R. Ha, S. Yoon, S. M. Jeong, H. Choi, D. W. Kang, *J. Power Sources.* **2020**, *453*, 227903.
[42] K. W. Jung, M. R. Sohn, H. M. Lee, I. S. Yang, S. Do Sung, J. Kim, E. Wei-Guang Diau, W. I. Lee, *Sustain Energy Fuels.* **2018**, *2*, 294.
[43] H. Zhu, M. Pan, M. B. Johansson, E. M. J. Johansson, *ChemSusChem.* **2017**, *10*, 2592.
[44] B. Ghosh, B. Wu, X. Guo, P. C. Harikesh, R. A. John, T. Baikie, A. T. S. W. Arramel, C. Guet, T. C. Sum, S. Mhaisalkar, N. Mathews, *Adv. Energy Mater.* **2018**, *8*, 1802051.
[45] M.-C. Wu, Q.-H. Wang, K.-C. Hsiao, S.-H. Chen, C.-M. Ho, M.-H. Jao, Y.-H. Chang, W.-F. Su, *Chem Eng J Adv.* **2022**, *10*, 100275.
[46] N. Pai, J. Lu, T. R. Gengenbach, A. Seeber, A. S. R. Chesman, L. Jiang, D. C. Senevirathna, P. C. Andrews, U. Bach, Y. B. Cheng, A. N. Simonov, *Adv. Energy Mater.* **2019**, *9*, 1803396.
[47] M. Righetto, S. Caicedo-Dávila, M. T. Sirtl, V. J.-Y. Lim, J. B. Patel, D. A. Egger, T. Bein, L. M. Herz, *J. Phys. Chem. Lett.* **2023**, *14*, 10340.
[48] L. R. V. Buizza, A. D. Wright, G. Longo, H. C. Sansom, C. Q. Xia, M. J. Rosseinsky, M. B. Johnston, H. J. Snaith, L. M. Herz, *ACS Energy Lett.* **2021**, *6*, 1729.
[49] M. Righetto, Y. Wang, K. A. Elmestekawy, C. Q. Xia, M. B. Johnston, G. Konstantatos, L. M. Herz, *Adv. Mater.* **2023**, *35*, 2305009.
[50] L. R. V. Buizza, H. C. Sansom, A. D. Wright, A. M. Ulatowski, M. B. Johnston, H. J. Snaith, L. M. Herz, *Adv. Funct. Mater.* **2022**, *32*, 2108392.
[51] B. Wu, W. Ning, Q. Xu, M. Manjappa, M. Feng, S. Ye, J. Fu, S. Lie, T. Yin, F. Wang, T. W. Goh, P. C. Harikesh, Y. K. E. Tay, Z. X. Shen, F. Huang, R. Singh, G. Zhou, F. Gao, T. C. Sum, *Sci. Adv.* **2021**, *7*, 3160.
[52] S. Lal, M. Righetto, A. M. Ulatowski, S. G. Motti, Z. Sun, J. L. MacManus-Driscoll, R. L. Z. Hoye, L. M. Herz, *J. Phys. Chem. Lett.* **2023**, *14*, 6620.
[53] R. A. Jagt, I. Bravić, L. Eyre, K. Gałkowski, J. Borowiec, K. R. Dudipala, M. Baranowski, M. Dyksik, T. W. J. van de Goor, T. Kreouzis, M. Xiao, A. Bevan, P. Płochocka, S. D. Stranks, F. Deschler, B. Monserrat, J. L. MacManus-Driscoll, R. L. Z. Hoye, *Nat. Commun.* **2023**, *14*, 2452.
[54] M. Khazaee, K. Sardashti, C. C. Chung, J. P. Sun, H. Zhou, E. Bergmann, W. A. Dunlap-Shohl, Q. Han, I. G. Hill, J. L. Jones, D. C. Lupascu, D. B. Mitzi, *J Mater Chem A Mater.* **2019**, *7*, 2095.
[55] V. Pecunia, Y. Yuan, J. Zhao, K. Xia, Y. Wang, S. Duhm, L. Portilla, F. Li, *Nanomicro Lett.* **2020**, *12*, 27.
[56] B. D. Viezbicke, S. Patel, B. E. Davis, D. P. Birnie, *Phys. Status Solidi B.* **2015**, *252*, 1700.
[57] X. Li, B. Traoré, M. Kepenekian, L. Li, C. C. Stoumpos, P. Guo, J. Even, C. Katan, M. G. Kanatzidis, *Chem. Mater.* **2021**, *33*, 6206.
[58] Y.-T. Huang, S. R. Kavanagh, M. Righetto, M. Rusu, I. Levine, T. Unold, S. J. Zelewski, A. J. Sneyd, K. Zhang, L. Dai, A. J. Britton, J. Ye, J. Julin, M. Napari, Z. Zhang, J. Xiao, M. Laitinen, L. Torrente-Murciano, S. D. Stranks, A. Rao, L. M. Herz, D. O. Scanlon, A. Walsh, R. L. Z. Hoye, *Nat. Commun.* **2022**, *13*, 4960.
[59] R. Hooijer, A. Weis, A. Biewald, M. T. Sirtl, J. Malburg, R. Holfeuer, S. Thamm, A. A. Y. Amin, M. Righetto, A. Hartschuh, L. M. Herz, T. Bein, *Adv. Opt. Mater.* **2022**, *10*, 2200354.
[60] M. Scholz, K. Oum, T. Lenzer, *Phys. Chem. Chem. Phys.* **2018**, *20*, 10677.
[61] V. Pecunia, J. Zhao, C. Kim, B. R. Tuttle, J. Mei, F. Li, Y. Peng, T. N. Huq, R. L. Z. Hoye, N. D. Kelly, S. E. Dutton, K. Xia, J. L. MacManus-Driscoll, H. Sirringhaus, *Adv. Energy Mater.* **2021**, *11*, 2003968.
[62] K. S. Song, R. T. Williams, *Self-Trapped Excitons*, 2nd ed., *105*, Springer, Berlin Heidelberg, Berlin, Heidelberg **1996**.
[63] V. M. Nield, D. A. Keen, W. Hayes, R. L. Mcgreevy, *Solid State Ion.* **1993**, *66*, 247.
[64] R. H. Victora, *Phys. Rev. B.* **1997**, *56*, 4417.
[65] C. Kittel, *Introduction to Solid State Physics*, 8th ed., Wiley, Hoboken, New Jersey, United States **2004**.
[66] N. Apsley, H. P. Hughes, *Philos. Mag.* **1974**, *30*, 963.
[67] T. Holstein, *Ann Phys.* **1959**, *8*, 343.
[68] C. Sun, Y. H. Guo, Y. Yuan, W. X. Chu, W. L. He, H. X. Che, Z. H. Jing, C. Y. Yue, X. W. Lei, *Inorg. Chem.* **2020**, *59*, 4311.
[69] E. Iliopoulos, D. Doppalapudi, H. M. Ng, *Appl. Phys. Lett.* **1998**, *73*, 375.
[70] S. Mukherjee, K. Sarkar, G. P. Wiederrecht, R. D. Schaller, D. J. Gosztola, M. A. Stroscio, M. Dutta, *Nanotechnology.* **2018**, *29*, 175201.
[71] D. S. Arteev, A. V. Sakharov, W. V. Lundin, E. E. Zavarin, D. A. Zakheim, A. F. Tsatsulnikov, *Semiconductors.* **2019**, *53*, 1900.
[72] B. Ghosh, B. Wu, H. K. Mulmudi, C. Guet, K. Weber, T. C. Sum, S. Mhaisalkar, N. Mathews, *ACS Appl. Mater. Interfaces.* **2018**, *10*, 35000.
[73] G. Whitfield, P. B. Shaw, *Phys. Rev. B.* **1976**, *14*, 3346.
[74] G. Tan, S. Hao, R. C. Hanus, X. Zhang, S. Anand, T. P. Bailey, A. J. E. Rettie, X. Su, C. Uher, V. P. Dravid, G. J. Snyder, C. Wolverton, M. G. Kanatzidis, *ACS Energy Lett.* **2018**, *3*, 705.
[75] W. Chen, D. Dahliah, G. M. Rignanese, G. Hautier, *Energy Environ. Sci.* **2021**, *14*, 3567.
[76] H. C. Sansom, L. R. V. Buizza, M. Zanella, J. T. Gibbon, M. J. Pitcher, M. S. Dyer, T. D. Manning, V. R. Dhanak, L. M. Herz, H. J. Snaith, J. B. Claridge, M. J. Rosseinsky, *Inorg. Chem.* **2021**, *60*, 18154.